Retrieving Atmospheric Thermodynamic and Hydrometeor Profiles Using a Thermodynamic-Constrained Kalman Filter 1D-Var Framework Based on Ground-based Microwave Radiometer

Qi Zhang[1,3], Tianmeng Chen[2]*, Jianping Guo[2]*, Yu Wu[4], Bin Deng[5], Junjie Yan[1,3]

[1]Key Open Laboratory of Intelligent Meteorological Observation Technology, China Meteorological Administration, Beijing, 100081, China
[2]State Key Laboratory of Severe Weather Meteorological Science and Technology & Specialized Meteorological Support Technology Research Center, Chinese Academy of Meteorological Sciences, Beijing 100081, China
[3]Engineering Technology Research and Development Center, China Huayun Meteorological Technology Group Co., Ltd., Beijing 100081, China
[4]Hainan Provincial Meteorological Observatory, Hainan, 570203, China
[5]Jiangxi Weather Modification Center, Nanchang, 330000, China

Correspondence to: Prof. Dr. Jianping Guo (jpguo@cma.gov.cn) and Dr. Tianmeng Chen (chentm@cma.gov.cn)

Abstract. Ground-based microwave radiometers (GMWRs) provide continuous thermodynamic profiling but suffer from degraded accuracy under cloudy and precipitating conditions when using classical one-dimensional variational (1D-Var) retrievals. To address this, we develop a thermodynamic-constrained Kalman filter variational framework (TCKF1D-Var) that enforces moist-thermodynamic consistency through the use of virtual potential temperature as the control variable, employs a ratio-based cost function independent of prescribed background and observation error covariances, and integrates a diagnostic microphysics closure to represent liquid and ice water. Validation over 44 GMWR sites in North China, including seven with collocated radiosondes, shows that TCKF1D-Var systematically reduces temperature and humidity biases relative to ERA5 (European Centre for Medium-Range Weather Forecasts Reanalysis version 5) and 1D-Var, with the largest improvements above 2 km for temperature and below 5.5 km for humidity. Temperature root-mean-square errors remain comparable to ERA5 and lower than 1D-Var below 8.5 km, while humidity errors are improved near the surface though degraded in the mid-troposphere due to vertical-resolution mismatch and channel cross-talk. Evaluation against collocated EarthCARE (Earth Clouds, Aerosols and Radiation Explorer) cloud liquid water content profiles demonstrates that TCKF1D-Var yields the lowest biases and errors and best reproduces observed distributions, confirming the benefit of the microphysics constraint. Case analyses of short-duration heavy rainfall further show that TCKF1D-Var enhances precursor signals of convection, extending the effective lead time for early warning relative to ERA5 and substantially outperforming 1D-Var. These results highlight the value of embedding physical constraints and microphysical closure within GMWR retrievals, offering a practical pathway to improve continuous thermodynamic monitoring and support high-impact weather nowcasting.

1 Introduction

High-resolution thermodynamic and hydrometeor profiles are essential for both atmospheric research and operational weather forecasting (Wulfmeyer et al. 2015; Wagner et al., 2019; Hu et al., 2019). Rapid vertical changes in temperature and water vapor associated with synoptic features can initiate high-impact weather events, including squall lines (Löhnert and Maier, 2012; Geerts et al., 2017) and mesoscale convective systems (Teixeira et al., 2025). Moreover, long-term, high-resolution datasets of temperature and humidity profiles in the PBL can help reveal how anthropogenic influences, such as urbanization, alter the thermodynamic structure (Barrera-Verdejo et al., 2021; Turner and Löhnert, 2021). Recognizing this need, the China Meteorological Administration (CMA) launched the "Weak-Link Remediation Project" in 2021, deploying ground-based microwave radiometers (GMWRs) and other instrumemts at selected sites to continuously retrieve high-resolution thermodynamic and hydrometeor profiles throughout the troposphere fill the observational gap between sparse radiosonde launches and satellite overpasses. This makes the GMWRs particularly valuable for monitoring fast-changing atmospheric signals and supporting short-range weather prediction.

However, the performance of GMWR retrievals strongly depends on atmospheric conditions. Under clear-sky conditions, GMWR observations generally provide reliable temperature and humidity profiles with reasonable accuracy compared to radiosondes, regardless of methodological differences (Weisz et al., 2013; Ebell et al., 2017; Adler et al., 2021; Li et al., 2021; Xu, 2024). In contrast, under non-clear-sky conditions, significant retrieval biases can arise. Clouds introduce additional scattering and emission, particularly liquid water clouds that affect the 22–31 GHz water vapor absorption band, leading to overestimation of humidity and distortion of the retrieved vertical distribution (Zhang et al., 2024; Viggiano et al., 2025). Likewise, precipitation causes strong attenuation and scattering in both water vapor and oxygen absorption channels, degrading the information content for temperature retrievals (Kummerow et al., 2002; Christofilakis et al., 2020). These effects reduce retrieval reliability, especially in the lower troposphere where cloud and precipitation impacts are strongest.

Consequently, although GMWRs remain indispensable for continuous thermodynamic profiling, their application under cloudy and precipitating conditions requires advanced retrieval frameworks to mitigate these limitations. In this study, we introduce a novel Kalman filter–based one-dimensional variational optimal estimation framework (TCKF1D-Var) that integrates a thermodynamic conservation–constrained cost function with a cloud microphysics parameterization scheme, which generates retrievals of temperature, humidity, and hydrometeor profiles from microwave radiometer observations with higher accuracy. A comprehensive comparison with classical one-dimensional variational (1D-Var) method demonstrates that the proposed approach substantially improves retrieval accuracy, highlighting both its methodological novelty and its effectiveness in producing high-quality atmospheric profile products.
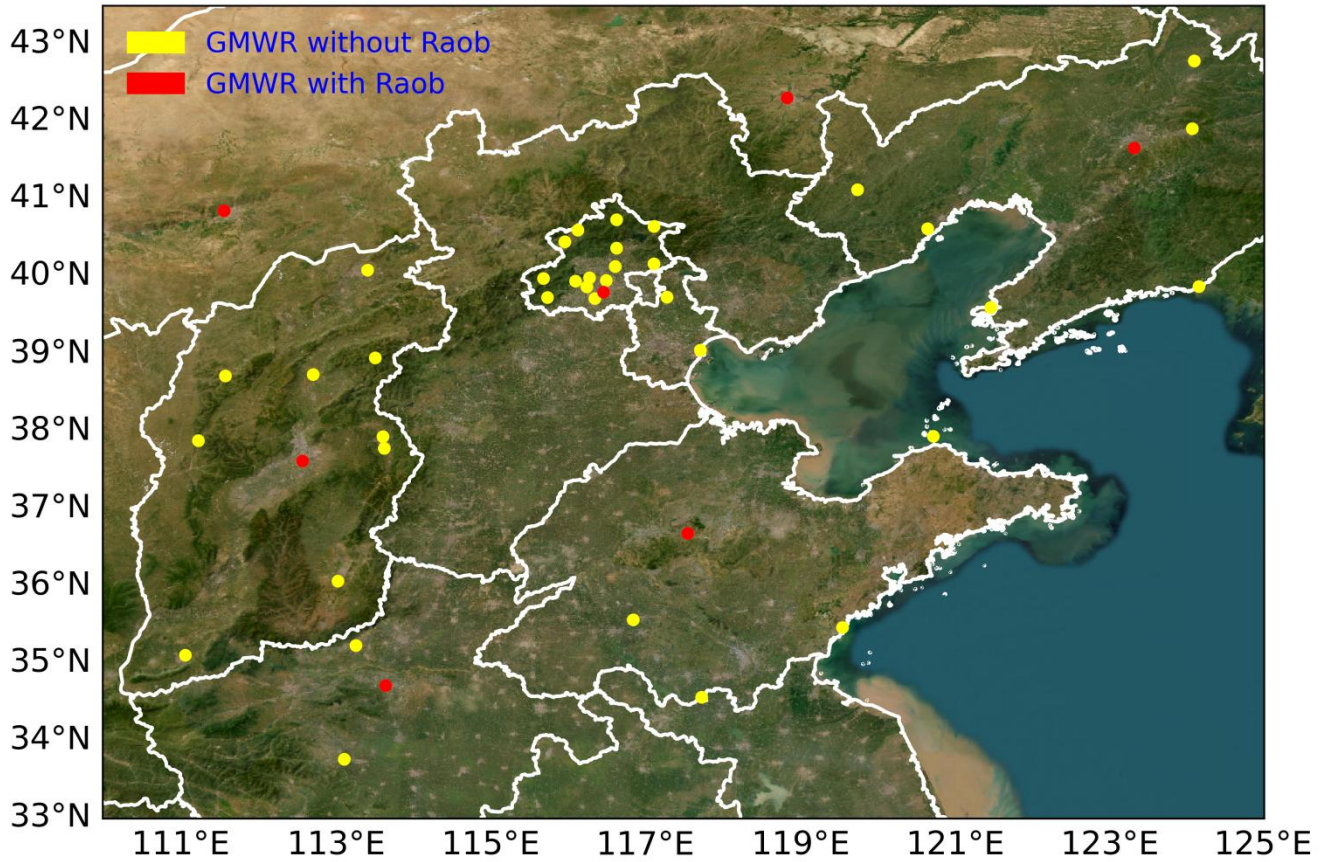
The remainder of this paper is organized as follows. Section 2 describes the study sites, instruments, and datasets employed. Section 3 presents the technical framework and implementation of the 1D-Var and TCKF1D-Var optimal estimation methods. Section 4 evaluates the accuracy of thermodynamic profiles retrieved by these three frameworks under both daytime and nighttime conditions, as well as under different weather scenarios. Finally, Section 5 provides a summary and discusses the implications of the results for future research.

2 Data

2.1 GMWR Observation

In the North China region, the GMWRs deployed at different sites originate from various manufacturers, yet their channel configurations are consistent. Each instrument is equipped with seven water vapor channels (22.240, 23.040, 23.840, 25.440, 26.240, 27.840, and 31.400 GHz) and seven oxygen channels (51.260, 52.280, 53.860, 54.940, 55.500, 56.660, and 58.000 GHz), dedicated to observing the vertical distribution of atmospheric water vapor and temperature, respectively. Figure 1 illustrates the spatial distribution of GMWRs across North China: in total, 44 stations are equipped with GMWRs under the supervision of the CMA, among which 7 stations are co-located with conventional radiosonde launches. Simulated brightness temperatures, calculated from radiosonde profiles at these 7 stations using the RTTOV-gb (Radiative Transfer for TOVS − ground-based) radiative transfer model (De Angelis et al., 2016; Cimini et al., 2019), were compared with GMWR observations. The results show that GMWR measurements agree well with radiosonde-based simulations under clear-sky and cloudy conditions, while larger discrepancies occur during fog and precipitation events (Figure 2). Therefore, in this study, all optimal estimation retrievals are restricted to clear-sky and cloudy conditions in order to ensure both retrieval reliability and retrieval applicability.

Figure 1. Spatial distribution of ground-based microwave radiometers (GMWRs) in North China. Yellow markers denote stations equipped only with GMWRs, while red markers indicate stations where GMWRs are co-located with radiosonde launches. The topographical basemap is retrieved from ArcGIS Online powered by Esri (Esri et al., 2025).
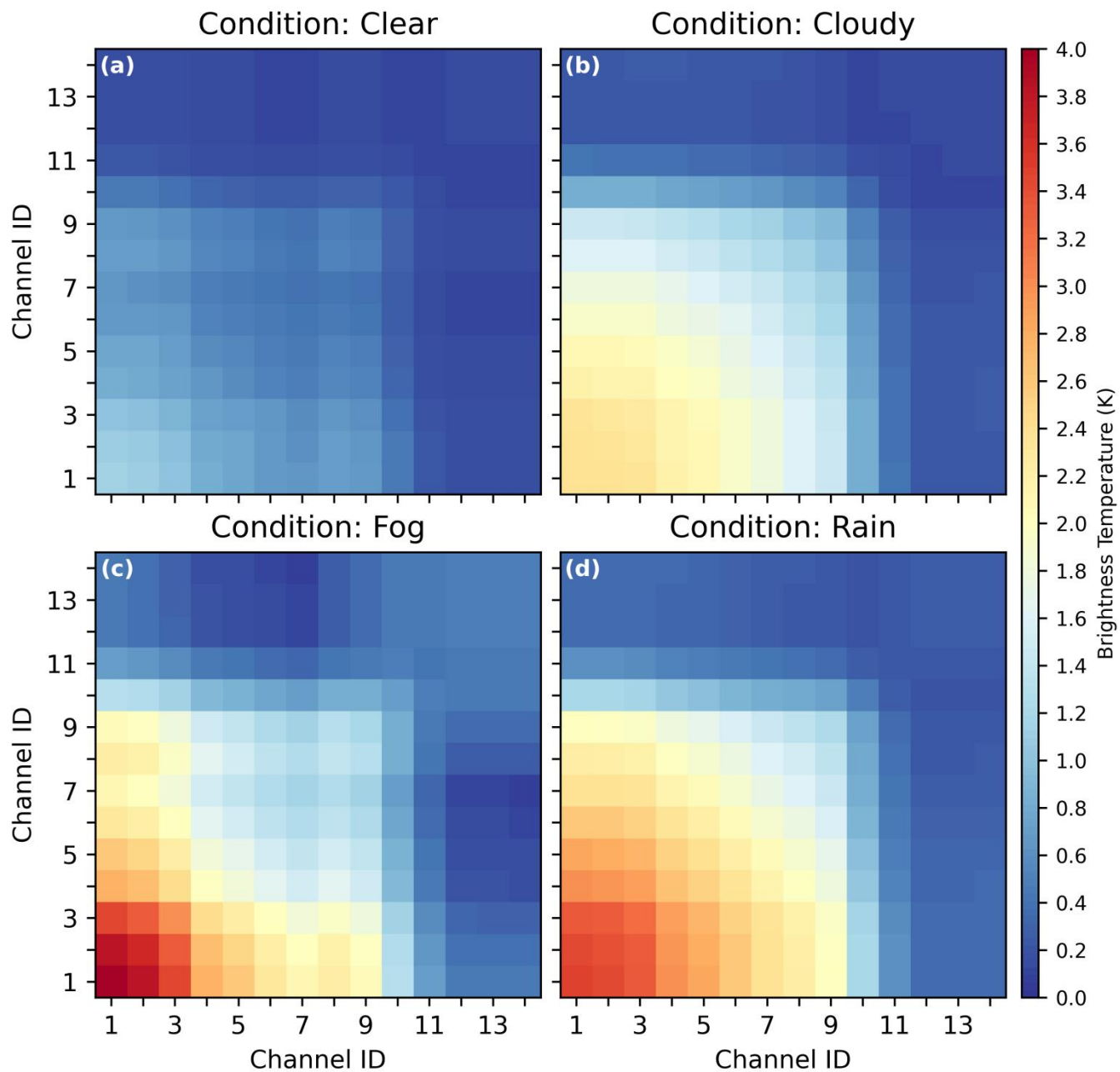
Figure 2. Square root of the error covariance matrices of brightness temperature differences between ground-based microwave radiometer (GMWR) observations and radiosonde-based simulations for different weather conditions: (a) clear-sky conditions, (b) cloudy conditions, (c) fog conditions, and (d) precipitation conditions.

2.2 Radiosonde

Two radiosondes are launched daily from stations 53463, 53772, 54218, 54340, 54511, 54727, and 57083 (red dots in Figure 1), typically around 23:15 and 11:15 UTC. These routine soundings are employed as reference ("truth") data for constructing observation error covariance matrices and for evaluating the retrieval accuracy. The radiosondes provide high-quality vertical profiles with well-documented instrumental characteristics: temperature is measured with a resolution of 0.1 K and an accuracy of 0.5 K, relative humidity with a resolution of 1% and an accuracy of 5%, and pressure with a resolution of 0.1 hPa and an accuracy of 0.5 hPa (Yao et al., 2025). Such specifications ensure that the radiosonde observations are sufficiently accurate to serve as an independent benchmark against which the ground-based microwave radiometer retrievals can be objectively assessed.

2.3 Hydrometeor Profile

To evaluate the performance of the optimal estimation framework for hydrometeor profiling, it is both sufficient and necessary to employ the EarthCARE (Earth Cloud, Aerosol, and Radiation Explorer, Kimura et al., 2003; Donovan et al., 2013; Hélière et al., 2017) cloud retrieval product (CPR_CLD_2A, Mason et al., 2024; Imura et al., 2025; European Space Agency, 2025) as a reference. The active radar observations from EarthCARE provide vertically resolved cloud liquid and ice water content with high sensitivity to optically thick clouds with radar reflective factor target accuracy less than 2.7dB, which ensures the sufficiency of this dataset as a benchmark for validating the vertical structures. Given the lack of long-term, ground-based observations with comparable vertical resolution and global coverage, the use of CPR_CLD_2A product is also a necessary step to establish the reliability and applicability of the optimal estimation hydrometeor retrievals in a broader context.

2.4 Priori Profile

In this study, the a priori atmospheric profile at each GMWR station is derived from the ERA5 reanalysis (Hoffmann et al., 2019; Hersbach et al., 2020; Bell et al., 2021) using a bilinear interpolation method. ERA5 is widely recognized as one of the most reliable global reanalysis products, providing high temporal (hourly) and spatial (0.25° × 0.25°) resolution fields as well as a consistent assimilation of a large variety of observations. These advantages make ERA5 an appropriate substitute for direct observations in regions or periods where in situ measurements are sparse, discontinuous, or completely unavailable. The use of ERA5 as background information ensures that the constructed priori profiles capture large-scale atmospheric variability with high fidelity, while still allowing the GMWR observations to provide additional fine-scale constraints during the retrieval process.

3 Methods

3.1 1D-Var Framework

As a widely used approach to retrieve atmospheric state, 1D-Var (Figure 3a) has been used in thermodynamic profile retrieval systems for both ground-based (Hewison and Gaffard, 2006; Martinet et al., 2017; Gamage et al., 2020), airbone (Thelen et al., 2009; Bell et al., 2021), and spacebone instruments (Noh et al., 2021; Wang et al., 2024; Carminati 2022) by minimizing the cost function (Rodgers, 2000) Eq. (1):

$$J_{(x)} = (x - x_0)^T B^{-1}(x - x_0) + (y - H_{(x)})^T R^{-1}(y - H_{(x)}) , \tag{1}$$

where y is the GMWR brightness temperature observation at a given time; R is the observation error covariance matrix; B is the background error covariance matrix; x_0 is the priori profile; and $H_{(x)}$ is the observation-operator-simulated brightness temperature corresponding to a given atmospheric state x. In this study, the RTTOV-gb is selected as the observation operator H.
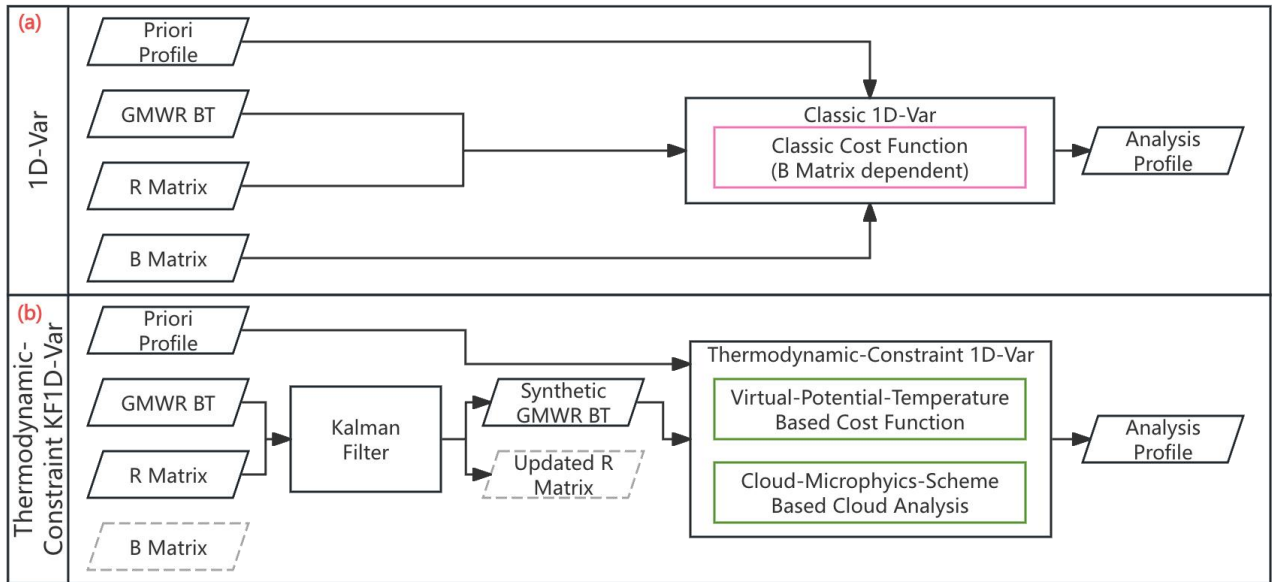

Figure 3. The workflow of 1D-Var (a) and TCKF1D-Var (b) Framework.

The accuracy of thermodynamic profiles retrieved with the 1D-Var framework depends not only on the measurement precision of the instruments but also on the specification of the background and observation error covariance matrices, which are typically estimated from long-term observational archives. While such climatologically based error covariances can

7

provide overall robust accuracy, their emphasis on representing the mean state reduces the ability of the retrieved optimal profiles to capture rapidly evolving weather phenomena, such as convective system initiation.

3.2 TCKF1D-Var Framework

The TCKF1D-Var framework (Figure 3b) inherits the Kalman filter's capability of reducing random measurement noise by generating synthetic observations (Welch and Bishop, 1995; Foth and Pospichal, 2017; Zhang et al., 2023, 2025) but replaces the cost function of the 1D-Var (Eq. 1) with a thermodynamic-constrained formulation in which the background and observation error covariance matrices are no longer required (Section 3.3.1). In addition, a microphysical hydrometeor analysis module (Section 3.3.2) is integrated into the 1D-Var framework to enhance the accuracy of the retrieved profiles under cloudy conditions.

3.2.1 Thermodynamic-Constrained Cost Function

Since virtual potential temperature (θ_v) accounts for the influences of air pressure (P), temperature (T), water vapor (q_v), and hydrometeors (q_l for cloud liquid water content, q_i for cloud ice water content) in its calculation (Eq. (2) and (3)) and is conserved during moist adiabatic processes in the atmosphere (de Haan and van der Veen, 2014; Benjamin et al., 2021), it serves as an ideal control variable in the cost function. In addition, using this control variable not only allows for the adjustment of temperature and humidity profiles based on observations but also enables simultaneous modifications to pressure and hydrometeor profiles. More importantly, compared to classic 1D-Var (Section 3.1), this control variable ensures that the retrieved profiles satisfy thermodynamic equilibrium while achieving the mathematical optimum of the cost function.

$$\theta_{v(x)} = T(\frac{P_o}{P})^K (1 + 0.61 q_v - q_l - q_i) , \tag{2}$$

$$K = \frac{R_d}{C_p} , \tag{3}$$

where R_d is the specific gas constant for dry air, and C_p is the specific heat capacity at constant pressure for dry air.

To eliminate the influence of climatological background and observation error covariance matrices on the retrieved profiles, while ensuring that both the observation and control variable terms in the cost function are dimensionless, we replace the classic difference-based calculation in the cost function with a ratio-based formulation. Additionally, to enhance the contribution of the initial analysis increment to the cost function and reduce the number of iterations, unity (1, in this case) is subtracted from both the observation and control variable terms before squaring. The newly formulated cost function is expressed as in Eq. (4):
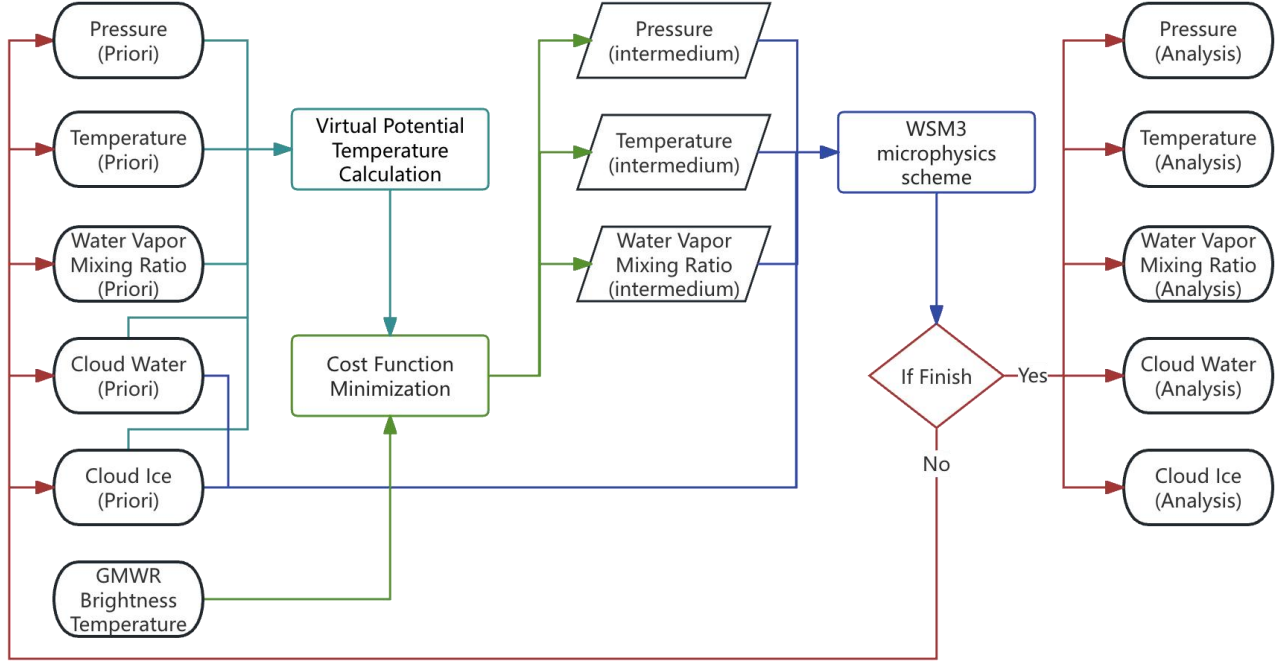
$$J_{(x)} = \left(\frac{H_{(x)}}{y} - 1\right)^2 + \left(\frac{\theta_{v(x)}}{\theta_{v(x_o)}} - 1\right)^2, \tag{4}$$

Due to the finite precision of floating-point arithmetic, a loss of significant digits may occur, potentially compromising the numerical stability of the computation. To mitigate this issue, both the observed ($H_{(x)}\big/y$) and simulated ($\theta_{v(x)}\big/\theta_{v(x_o)}$)

165 variables are normalized to the range of −1 to 1 using an amplification factor derived from $max(abs(1\left|\frac{H_{(x)}}{y} - 1\right.), abs(1\left|\frac{\theta_{v(x)}}{\theta_{v(x_o)}} - 1\right.))$, where $max()$ and $abs()$ denote the maximum and absolute value operators, respectively. Furthermore, all input values are converted to double precision before the initialization of the minimization algorithm to enhance numerical stability and robustness. To avoid normalization issues when observed and simulated brightness temperatures are very close to each other, the quality control module automatically discards GMWR

170 channel observations whose brightness temperature departures from the simulated values are smaller than the noise-equivalent temperature difference. In addition, the ratio-based cost function provides several advantages over the conventional difference-based formulation used in standard 1D-Var retrievals. It ensures balanced channel weighting, as each channel is normalized by its own magnitude and channels with smaller brightness temperatures are no longer underrepresented during optimization. It also achieves better physical consistency, since the ratio-based form is closer to the

175 logarithmic radiative response of microwave observations, making the inversion more physically meaningful. Finally, it offers enhanced robustness to calibration biases, being less sensitive to multiplicative gain or calibration errors and therefore improving retrieval performance under low signal-to-noise conditions.

3.2.2 Microphysical Hydrometeor Analysis

While RTTOV-gb incorporates the influence of cloud liquid water in brightness temperature calculations and provides the

180 corresponding Jacobians, the inherently discontinuous vertical structure of clouds in the real atmosphere prevents liquid water profiles from being retrieved in a manner consistent with temperature and humidity profiles. Moreover, RTTOV-gb accounts only for liquid water, neglecting the impact of cloud ice. As a result, constructing the observational term of the cost function solely with RTTOV-gb is insufficient to ensure its physical consistency and closure. Therefore, the inclusion of a cloud microphysics scheme in the cost function is essential to achieve a physically consistent and closed formulation.

185 Considering the trade-off between computational efficiency and simulation accuracy, the WSM3 single-moment microphysics scheme (Hong et al., 2004; Que et al., 2016) is employed as the basis for the diagnostic representation of cloud liquid water and cloud ice profiles. The coupling between the thermodynamic constraint and the WSM3 single-moment microphysics scheme is illustrated in Figure 4. The procedure begins with the calculation of the virtual potential temperature from the priori thermodynamic and hydrometeor profile. These fields serve as the initial state for the cost function

190 minimization, where the cost function iteratively adjusts the pressure, temperature, and water vapor mixing ratio using the GMWR brightness temperature observations to produce intermedium profiles. The WSM3 microphysics scheme then

9

dynamically updates the cloud water and cloud ice mixing ratios based on the intermediate pressure, temperature, and water vapor profiles, together with the priori hydrometeor fields. This coupling ensures physical consistency between the thermodynamic state and the microphysical processes during each iteration. If the convergence criterion is satisfied, the resulting profiles of temperature, humidity, and hydrometeors are designated as the final analysis. Otherwise, the updated fields are fed back into the next iteration as new initial conditions until convergence is achieved.

Figure 4. Schematic of the coupling between the thermodynamic constraint and the WSM3 single-moment microphysics scheme. The cost function iteratively adjusts pressure, temperature, and water vapor using GMWR observations, while WSM3 updates cloud water and ice mixing ratios. The process repeats until convergence, yielding the final analysis of thermodynamic and hydrometeor profiles.
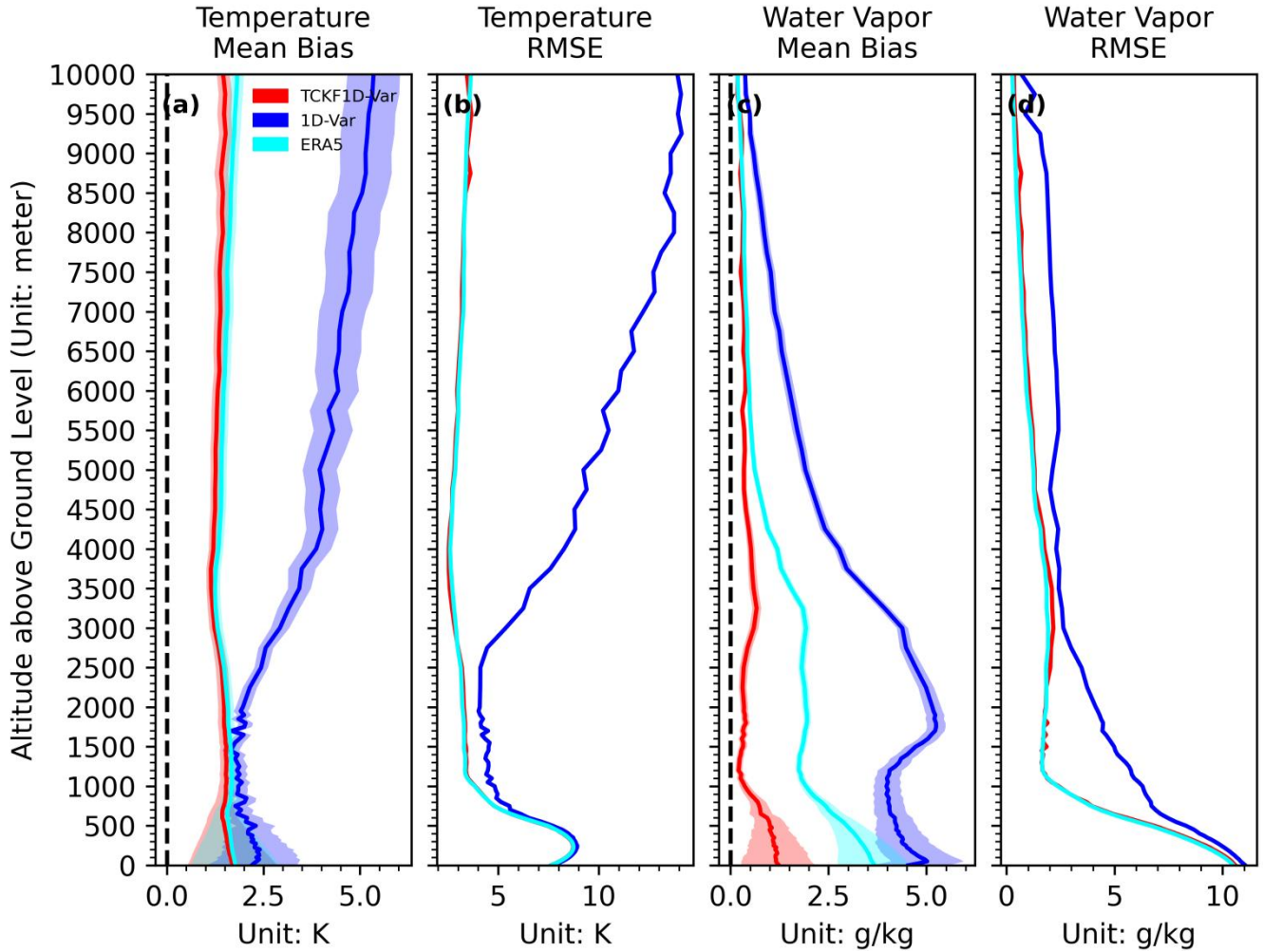
3.3 Cost Function Minimization

For the three frameworks described above, we employ the L-BFGS method (Limited-memory Broyden-Fletcher-Goldfarb-Shanno, Liu and Nocedal, 1989; Byrd et al., 1995) to obtain their optimal estimates. The rationale for choosing this method is as follows: (1) it has low memory requirements, making it suitable for high-dimensional optimization problems; (2) it does not explicitly store the Hessian matrix, but instead approximates it using the gradients and variable changes from the most recent m steps, resulting in fast convergence. In this study, all three frameworks share the same parameter settings: a maximum of 1500 iterations, a cost function convergence tolerance of 3×10^{-9}, a gradient norm convergence tolerance of 1×10^{-5}, and a maximum of 20 line searches per iteration.

10

4 Results and disscussion

4.1 Thermodynamic Profile Evaluation

4.1.1 General Performance

Figure 5 presents the validation results of TCKF1D-Var and 1D-Var, and the a priori profiles (ERA5) against radiosonde observations. As shown in Figure 5a, in terms of mean bias, the temperature profiles retrieved by TCKF1D-Var exhibit smaller average errors than the ERA5 a priori profiles, whereas the profiles derived from 1D-Var show larger mean bias than the a priori. This indicates that TCKF1D-Var is capable of effectively correcting the systematic biases in the ERA5 temperature profiles, while the corrections achieved by 1D-Var are less evident. Moreover, the bias reduction provided by TCKF1D-Var is more pronounced in the free atmosphere (above 2000 m) than within the boundary layer (below 2000 m). In terms of root mean square error (RMSE, Figure 5b), the random errors of the TCKF1D-Var temperature profiles are comparable to those of the ERA5 a priori below 8500 m above ground level, but become larger than the a priori above that level. Nevertheless, the overall random errors of TCKF1D-Var remain smaller than that from 1D-Var, highlighting that the TCKF1D-Var framework, which incorporates virtual potential temperature conservation, is more suitable for tropospheric temperature profile retrievals compared to 1D-Var framework. For water vapor, the improvement in mean bias correction achieved by TCKF1D-Var is even more evident than for temperature (Figure 5c). Within 0–1000 m, the mean bias of TCKF1D-Var water vapor profiles is below 1.5 g/kg, whereas the ERA5 a priori bias exceeds 1.5 g/kg. Between 1000–5500 m, TCKF1D-Var reduces the mean bias to below 0.5 g/kg, while the ERA5 a priori bias remains between 0.5 and 1.5 g/kg. In contrast, the water vapor profiles produced by 1D-Var show mean biases consistently larger than 0.5 g/kg below 9000 m. These results clearly demonstrate that, relative to 1D-Var, the TCKF1D-Var framework not only provides a more suitable approach for tropospheric temperature retrievals but also substantially reduces the mean bias of a priori water vapor profiles. Regarding RMSE (Figure 5d), the random errors of water vapor profiles retrieved with TCKF1D-Var are smaller than those of 1D-Var in the 0–1500 m range, but remain larger than the ERA5 a priori. In the 1500–5500 m layer, TCKF1D-Var exhibits the largest RMSE among all products, while in the 5500–10000 m layer, its random errors are comparable to those of 1D-Var but still higher than those of the a priori.

Figure 5. Validation of temperature and water vapor profiles retrieved by TCKF1D-Var (red), ERA5 a priori (cyan), and 1D-Var (blue) against radiosonde observations. The shaded areas denote the 95% confidence intervals that have passed the significance test. For temperature, TCKF1D-Var reduces the mean bias (pannel a) relative to the a priori and yields smaller overall random errors (pannel b) than 1D-Var. For water vapor, TCKF1D-Var substantially decreases the mean bias (pannel c) compared to the a priori, particularly below 5500 m, while its random errors (pannel d) are smaller than 1D-Var near the surface but remain larger than the a priori aloft.
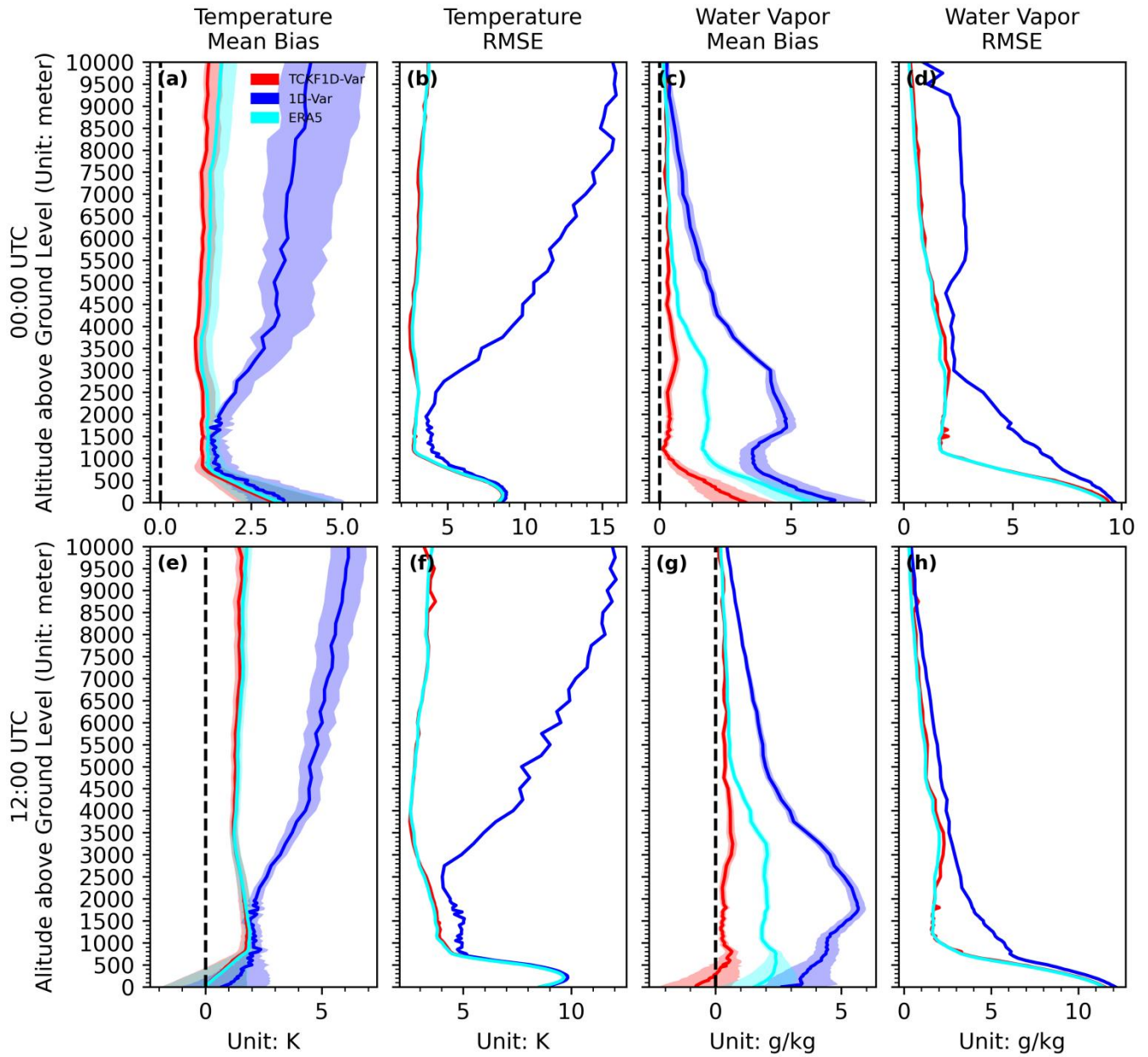
4.1.2 Day-Night Performance Difference

Building on Section 4.1.1, we further separate the validation results of the four sets of profiles against radiosonde observations at 00:00 UTC (08:00 BJT) and 12:00 UTC (20:00 BJT) to examine the diurnal variability in the performance of TCKF1D-Var and 1D-Var, and the ERA5 a priori profiles. For temperature mean bias, the differences between the TCKF1D-Var and ERA5 are predominantly limited within the boundary layer, while detectable improvements are found above 3000 m above ground level. As shown in Figure 6a, at 00:00 UTC, the temperature profiles from TCKF1D-Var exhibit smaller systematic biases than the ERA5 a priori, indicating a more effective correction of the a priori bias, while the

1D-Var bias is larger. At 12:00 UTC (Figure 6e), both TCKF1D-Var and the a priori show smaller mean biase than 1D-Var. Although the difference between TCKF1D-Var and the a priori becomes less pronounced during daytime, the TCKF1D-Var
250   bias remains lower than that of the a priori. For RMSE, the 00:00 UTC results (Figure 6b) are generally consistent with those in Section 4.1.1. However, at night (Figure 6f), the random errors of the TCKF1D-Var temperature profiles increase substantially above 8500 m, changing from being comparable to ERA5 during daytime to slightly higher than those of ERA5. Regarding water vapor mean bias (Figures 6c and 6g), the diurnal validation results are largely consistent with those in Section 4.1.1. The main difference appears below 500 m during nighttime, where, based on the 00:00 UTC radiosondes,
255   TCKF1D-Var shows positive mean bias, while at night the mean bias becomes negative. Similarly, for RMSE (Figures 6d and 6h), the overall behavior resembles that in Section 4.1.1, with the only notable difference occurring above 5500 m during daytime: based on the 00:00 UTC radiosondes, 1D-Var produces larger random errors than TCKF1D-Var, whereas at night the two are nearly indistinguishable.

Figure 6. Validation of temperature and water vapor profiles retrieved by TCKF1D-Var (red), ERA5 a priori (cyan), and 1D-Var (blue) against radiosonde observations at 00:00 UTC (a–d) and 12:00 UTC (e–h). The shaded areas denote the 95% confidence intervals that have passed the significance test. Panels (a, e) show mean temperature bias, indicating that TCKF1D-Var provides the most effective correction of systematic errors relative to the a priori. Panels (b, f) present temperature RMSE, where TCKF1D-Var maintains smaller random errors than 1D-Var during daytime, but shows increased errors above 2000 m at night. Panels (c, g) show mean water vapor bias, with TCKF1D-Var substantially reducing systematic errors compared to the other methods, while differences between 1D-Var are most evident above 5500 m. Panels (d, h) depict water vapor RMSE, again showing improved performance of TCKF1D-Var near the surface, with daytime differences between 1D-Var diminishing at night.

14

4.1.3 Accuracy under Different Weather Conditions

Under clear-sky and cloudy conditions (Figure 7a and e), the mean temperature errors are generally consistent with the results in Figure 5a, with TCKF1D-Var showing smaller biases than both ERA5 (as the background profiles) and 1D-Var. Under foggy (Figure 7i) and rainy (Figure 7m) conditions, TCKF1D-Var also exhibits reduced temperature errors below 5 km compared to ERA5 and 1D-Var, while above 5 km its performance is comparable to 1D-Var. In contrast, ERA5 shows similar errors to 1D-Var below 3 km but becomes less accurate above this level. Across all four weather regimes (clear-sky, cloudy, foggy, and rainy), the root-mean-square errors (RMSEs) of the temperature profiles are consistent with Fig. 5b, i.e., TCKF1D-Var performs comparably to ERA5 but clearly outperforms 1D-Var. For water vapor, under clear-sky (Figure 7c) and cloudy (Figure 7g) conditions, the mean errors of TCKF1D-Var remain smaller than those of ERA5 and 1D-Var, consistent with the results reported earlier. Under foggy (Figure 7k) and rainy (Figure 7o) conditions, TCKF1D-Var again yields smaller mean errors than both ERA5 and 1D-Var, although ERA5 exhibits larger biases than 1D-Var within the boundary layer (below ~500 m in foggy cases and below ~1000 m in rainy cases). In all four weather regimes, the RMSEs of water vapor profiles from TCKF1D-Var are comparable to those of ERA5 and consistently lower than those of 1D-Var.
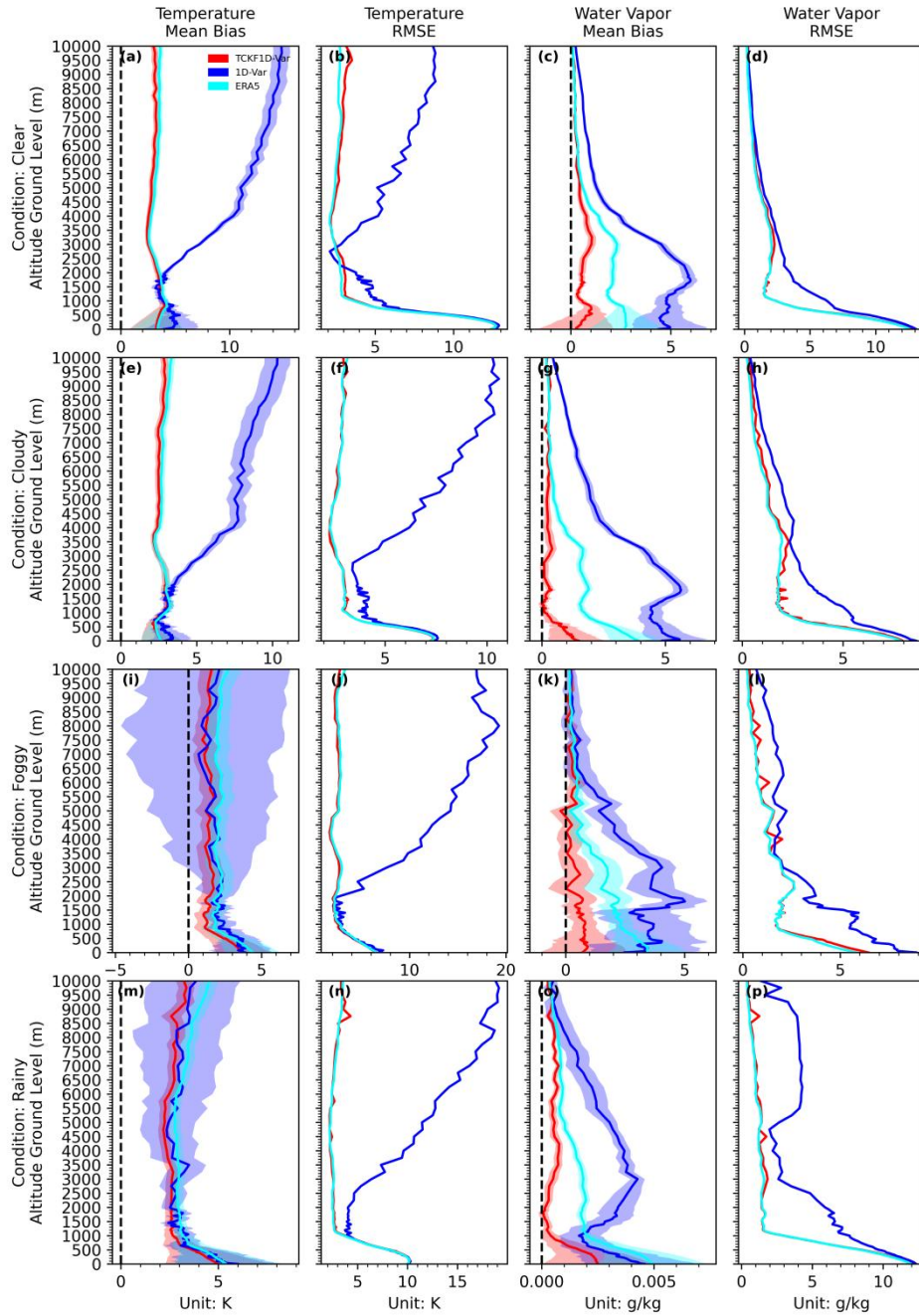
15

Figure 7. Mean errors (a, e, i, n) and root-mean-square errors (b, f, j, o for temperature; c, g, k, p for water vapor) of retrieved profiles under four weather conditions: clear-sky, cloudy, foggy, and rainy. The shaded areas denote the 95% confidence intervals that have passed the significance test. TCKF1D-Var consistently shows smaller temperature biases than ERA5 and 1D-Var below 5 km, with performance comparable to ERA5 above this level. ERA5 exhibits higher errors than 1D-Var above 3 km. For water vapor, TCKF1D-Var outperforms both ERA5 and 1D-Var across all regimes, while ERA5 displays larger boundary-layer errors (below ~500 m in foggy cases and below ~1000 m in rainy cases). In all conditions, the RMSEs of TCKF1D-Var are comparable to ERA5 and lower than 1D-Var.

16

4.1.4 Water Vapor RMSE Deficit Analysis

Despite the overall accuracy improvements achieved by the TCKF1D-Var framework, the retrieved water vapor profiles still exhibit systematic degradation in the middle troposphere (approximately 1.5–4.5 km) from the aspect of RMSE. A primary cause of this problem is the inherent coupling between temperature and humidity signals in the GMWR-measured brightness temperatures. While oxygen channels provide constraints on the temperature structure, their weighting functions peak at vertical levels, calculated by PyRTlib (Python package for non-scattering line-by-line microwave radiative transfer simulations, Larosa et al., 2024) using US Standard Atmosphere profile as background (NOAA, 1976), do not coincide with those of the water vapor channels (Figure 8). This vertical resolution mismatch leads to a partial leakage of temperature uncertainties into the humidity retrieval, thereby amplifying errors in this altitude range. The effect is particularly pronounced where temperature-sensitive channels show weak sensitivity, while humidity-sensitive channels remain reasonably responsive, leaving the retrieval under-constrained and more dependent on the completeness of the cost function design. Such temperature – humidity coupling has been reported in earlier radiative transfer and retrieval studies (e.g., Hewison, 2007; Löhnert and Maier, 2012), underscoring the necessity of explicitly characterizing vertical resolution mismatches and accounting for cross-variable error propagation when developing retrieval strategies. By contrast, a similar RMSE degradation is not observed in the temperature profiles. This asymmetry arises because the oxygen channels provide stronger and more vertically distinct weighting functions, which dominate the temperature information content and are only weakly influenced by humidity-related uncertainties. Furthermore, humidity channels have comparatively limited indirect sensitivity to temperature, and thus cannot introduce significant contamination into the temperature solution. As a result, the temperature retrieval remains well constrained across the troposphere, preventing the amplification of mid-level RMSE seen in the humidity retrieval.
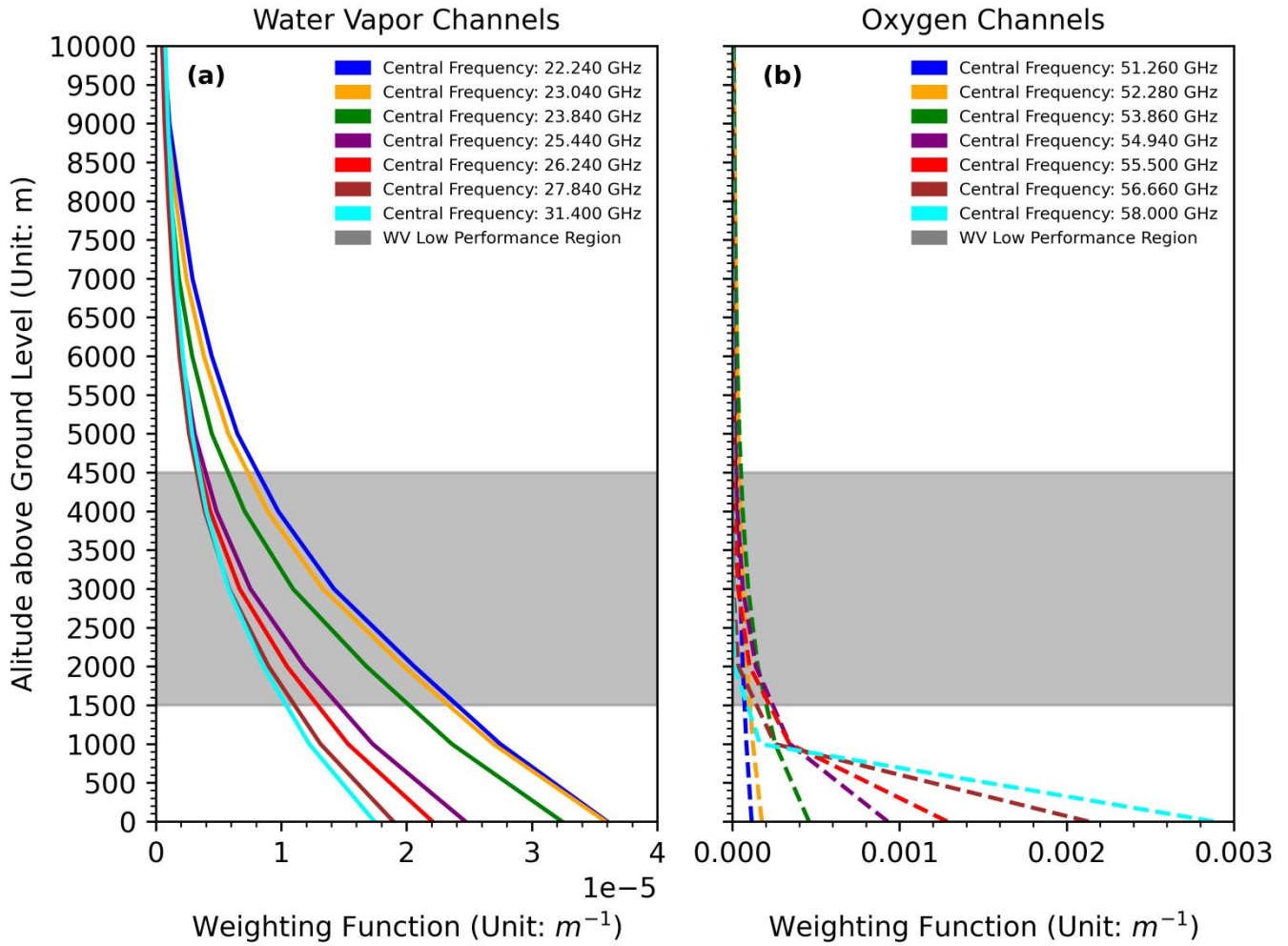
Figure 8. Weighting functions of temperature-sensitive (oxygen) and humidity-sensitive (water vapor) channels calculated with PyRTlib using the US Standard Atmosphere profile (NOAA, 1976) as background. The mismatch in vertical sensitivity between oxygen and water vapor channels is highlighted.

4.2 Hydrometeor Profile Evaluation

Previous evaluations of temperature and humidity have demonstrated the higher accuracy of the TCKF1D-Var profiles. In this section, we further validate the three retrieval products against the EarthCARE cloud liquid water content (CLWC) observations. The EarthCARE profiles were collocated in time and space by applying the following criterion: if an EarthCARE observation occurred within ±15 min of the profile validation time and within a 15 km radius of the station, the corresponding EarthCARE CLWC profile was used as the reference truth. Table 1 summarizes the number of collocated cases and profiles available in July 2025.

Table 1. Summary of collocated EarthCARE cloud liquid water content (CLWC) profiles and corresponding retrieval cases used for validation in July 2025.

WMO Station ID	Latitude (degree north)	Longitude (degree east)	Evaluation Profile Amount
53487	40.08	113.42	2
53662	38.72	111.58	2
53982	35.23	113.27	2
54398	40.13	116.62	2
54406	40.45	115.97	2
54412	40.73	116.63	2
54433	39.95	116.50	2
54505	39.94	116.10	2
54514	39.87	116.25	2
54594	39.72	116.35	4
54751	37.94	120.73	2
57171	33.77	113.12	4
53588	38.95	113.52	2
53673	38.73	112.72	4
53760	37.88	111.23	4
53959	35.11	111.07	4
54399	39.98	116.28	2
54410	40.60	116.13	2
54419	40.37	116.63	2
54424	40.17	117.12	4
54501	39.98	115.69	3
54511	39.80	116.47	2
54525	39.73	117.28	8
54727	36.68	117.55	2
58025	34.57	117.73	4

325   As shown in Figure 9, the mean errors indicate that the 1D-Var retrieval underestimates LWC by $10^1 – 10^2$ mg·m^{-3} relative to EarthCARE in the 0–6 km layer, while ERA5 shows a smaller underestimation of about $10^0 – 10^1$ mg·m^{-3}. In contrast, TCKF1D-Var exhibits the smallest bias, with deviations consistently within 10^0 mg·m^{-3} throughout the 0–6 km range. In terms of RMSE, TCKF1D-Var maintains values below 10^2 mg·m^{-3} across 0–6 km, whereas ERA5 exceeds 10^2 mg·m^{-3} except below 1 km, and 1D-Var shows the largest errors, remaining in the range of 10^2–10^3 mg·m^{-3}.
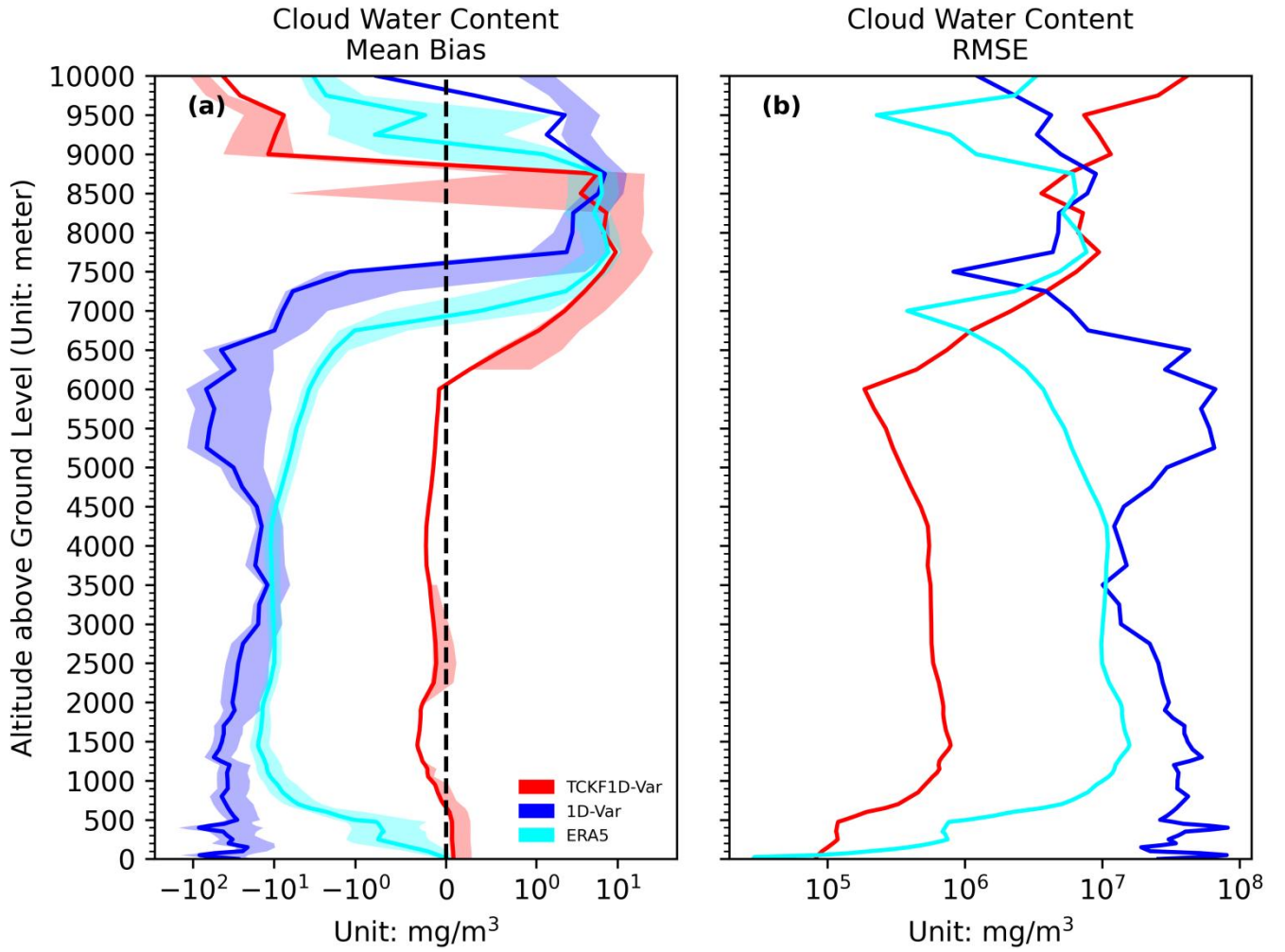
Figure 9. Mean error and root-mean-square error (RMSE) of cloud liquid water content (CLWC) profiles from 1D-Var, ERA5, and TCKF1D-Var relative to EarthCARE observations. The shaded areas denote the 95% confidence intervals that have passed the significance test. The 1D-Var retrievals show the largest underestimation (10^1–10^2 mg·m⁻³) and highest RMSE (10^2–10^3 mg·m⁻³), ERA5 exhibits smaller biases (10^0–10^1 mg·m⁻³) but RMSEs above 10^2 mg·m⁻³ except below 1 km, while TCKF1D-Var achieves the smallest deviations, with mean errors within 10^0 mg·m⁻³ and RMSEs consistently below 10^2 mg·m⁻³.

Histogram bins in Figure 10 are defined to ensure sufficient sample counts in each interval for robust frequency comparisons, following established practice in cloud-microphysics statistical analyses (Zhang et al., 2021; Mroz et al., 2023). The resulting CLWC frequency distributions (Figure 10) further substantiate the comparative findings: TCKF1D-Var aligns most closely with EarthCARE observations below 136 mg/m³, with particularly strong agreement in the 36–136 mg/m³ range. In the 0–34 mg/m³ interval, TCKF1D-Var differs from EarthCARE by roughly one order of magnitude (10^1), whereas ERA5 and 1D-Var exhibit discrepancies exceeding 10^2. For 136–170 mg/m³, the deviations of TCKF1D-Var relative to EarthCARE become comparable to, or slightly larger than, those of ERA5 and 1D-Var.

20

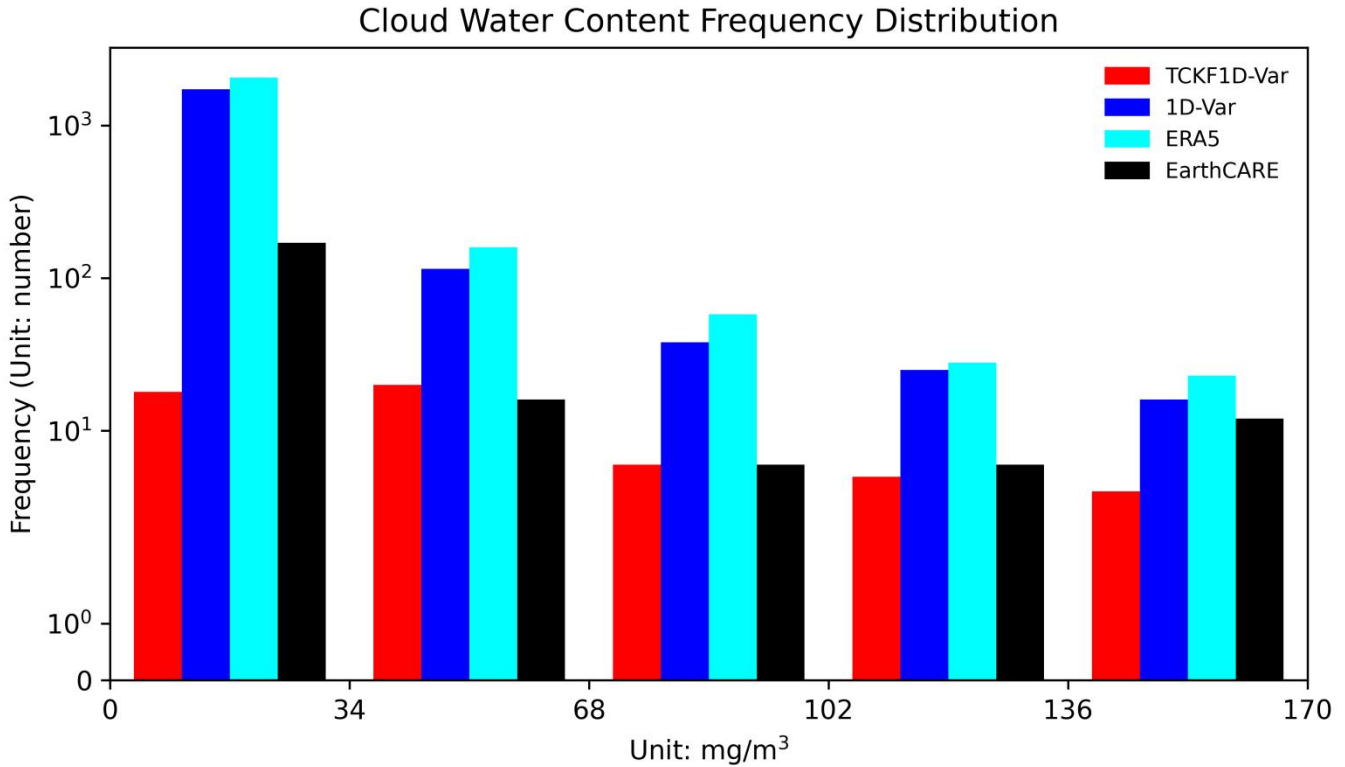## Cloud Water Content Frequency Distribution

Figure 10. Frequency distribution histograms of cloud liquid water content (CLWC) from 1D-Var, ERA5, and TCKF1D-Var compared with EarthCARE observations. TCKF1D-Var agrees most closely with EarthCARE below 136 mg·m^{-3}, particularly in the 36−136 mg·m^{-3} interval. In the 0−34 mg·m^{-3} range, TCKF1D-Var differs from EarthCARE by about one order of magnitude (10^1), while ERA5 and 1D-Var show larger discrepancies exceeding 10^2. For 136−170 mg·m^{-3}, the deviations of TCKF1D-Var relative to EarthCARE are comparable to, or slightly greater than, those of ERA5 and 1D-Var.

4.3 Extreme Precipitation Event Early-warning Capability Demonstration

The preceding results demonstrate that the thermodynamic profiles retrieved from TCKF1D-Var framework exhibit smaller mean biases than ERA5, with root-mean-square errors lower than those from 1D-Var and comparable to ERA5, while the retrieved cloud liquid water content shows a higher degree of consistency with EarthCARE observations compared to both 1D-Var and ERA5. To further confirm that these improvements in retrieval accuracy translate into practical benefits, we investigate their implications for the early identification of extreme precipitation signals. Using the criterion of hourly accumulated precipitation exceeding 10 mm to define heavy rainfall events (World Meteorological Organization, 2007), we identified eight short-duration extereme precipitation cases in July 2025 at stations equipped with GMWRs (Table 2). Following the approach proposed by Taylor et al. (2007) and Garcia-Carreras et al. (2010), we adopt the temporal moving anomaly of virtual potential temperature as an early-warning indicator, which removes slowly varying background signals associated with large-scale processes and diurnal variations. Using the selected precipitation cases, we analyze the time

360   series derived from different profile products and evaluate its relationship with the onset of heavy rainfall events. The temporal deviation of virtual potential temperature is calculated as follows:

$$\theta_v^{anomaly} = \theta_v^{T_0} - \frac{\sum_{t=T_0-Window\ Size}^{T_0} \theta_v^t}{Window\ Size},$$ (5)

where $\theta_v^{anomaly}$ is the temporal moving anomaly of virtual potential temperature, $\theta_v^{T_0}$ is the virtual potential temperature at observation time T_0, θ_v^t is the virtual potential temperature at time t within the time window of $Window\ Size$.

365   **Table 2. List of short-duration extreme precipitation cases (hourly accumulation >10 mm) observed in July 2025 at stations equipped with GMWRs.**

WMO Station ID	Start Date and Time (UTC)	End Date and Time (UTC)	Maximum Precipitation (mm/hr)
54727	2025-07-01 19:00:00	2025-07-01 21:00:00	13.7
57083	2025-07-01 17:00:00	2025-07-01 17:00:00	11.0
53772	2025-07-07 07:00:00	2025-07-07 07:00:00	15.5
53673	2025-07-09 17:00:00	2025-07-09 19:00:00	17.0
54727	2025-07-23 04:00:00	2025-07-23 04:00:00	14.5
53463	2025-07-25 07:00:00	2025-07-25 08:00:00	12.8
54511	2025-07-27 17:00:00	2025-07-27 19:00:00	10.4
54511	2025-07-28 20:00:00	2025-07-28 20:00:00	12.2

Figure 11 presents the case-averaged time–height evolution of the virtual potential temperature anomaly derived from ERA5 (Figure 11a, d, and g), TCKF1D-Var (Figure 11b, e, and h), and 1D-Var (Figure 11c, f, and i) under different temporal

370   averaging windows: 9.0-hour (Figure 11a, b, and c), 10.5-hour (Figure 11d, e, and f), and 12.0-hour (Figure 11g, h, and i), spanning from 11 hours prior to the onset of precipitation to the time of rainfall occurrence. From the ERA5 profiles, a distinct signal emerges below 400 m, where the anomaly changes from positive to negative during the 11 h preceding precipitation, accompanied by the intrusion of a warm anomaly tongue between 400 and 1100 m. Taking the transition from +0.25 K to −0.25 K as the early-warning threshold, ERA5 allows the identification of heavy rainfall 6–7 hour in advance.

375   When using the criterion of the anomaly dropping below −0.75 K as a secondary trigger, ERA5 can reconfirm the occurrence of heavy rainfall 4–5 hour ahead. The TCKF1D-Var retrievals reproduce these key precursory features, namely the positive-to-negative anomaly transition and the warm tongue intrusion, with an even stronger signal compared to ERA5. Based on the +0.25 K to −0.25 K transition, TCKF1D-Var indicates the potential onset of heavy rainfall 7.5–8.0 hour in advance, while the secondary threshold of −0.75 K enables a reconfirmation 4.0–4.5 hour before the event. By contrast, the

380   1D-Var profiles fail to capture the anomaly transition and warm tongue intrusion in the pre-precipitation stage, and the +0.25 K to −0.25 K transition cannot be identified as a reliable precursor. Moreover, when adopting the −0.75 K criterion, the 1D-

22

Var time–height series exhibits two spurious anomaly layers, leading to an increased false-alarm rate. In summary, the TCKF1D-Var framework enhances the representation of vertical atmospheric structures relevant to heavy rainfall initiation, such as the temporal evolution of virtual potential temperature anomalies and warm tongue intrusions, thereby providing a slightly longer lead time for early-warning signals compared to ERA5, whereas such improvements are absent in the 1D-Var results. Using the same methodology, we recalculated the time – height evolution of the virtual potential temperature anomaly with a reduced temporal averaging window (Figure A1 in Appendix A), and the gradients of the anomaly variations become weaker compared to those in Figure 11, owing to the shorter averaging window. Nevertheless, both ERA5 and TCKF1D-Var profiles still exhibit the characteristic transition of the anomaly from positive to negative about 7 – 8 h prior to rainfall onset. Although the warm anomaly tongue intrusion remains detectable in both products, its intensity is reduced. When adopting −0.75 K as the early-warning threshold, the signal becomes indistinct under the 4.5-hour averaging window, whereas it is enhanced and temporally stabilized within about 2 hours of the precipitation onset when using 6.0-hour and 7.5-hour windows. Consistent with the previous findings, the 1D-Var (Figure A1 c, f, and i) profiles fail to extract effective early-warning signals for heavy rainfall.
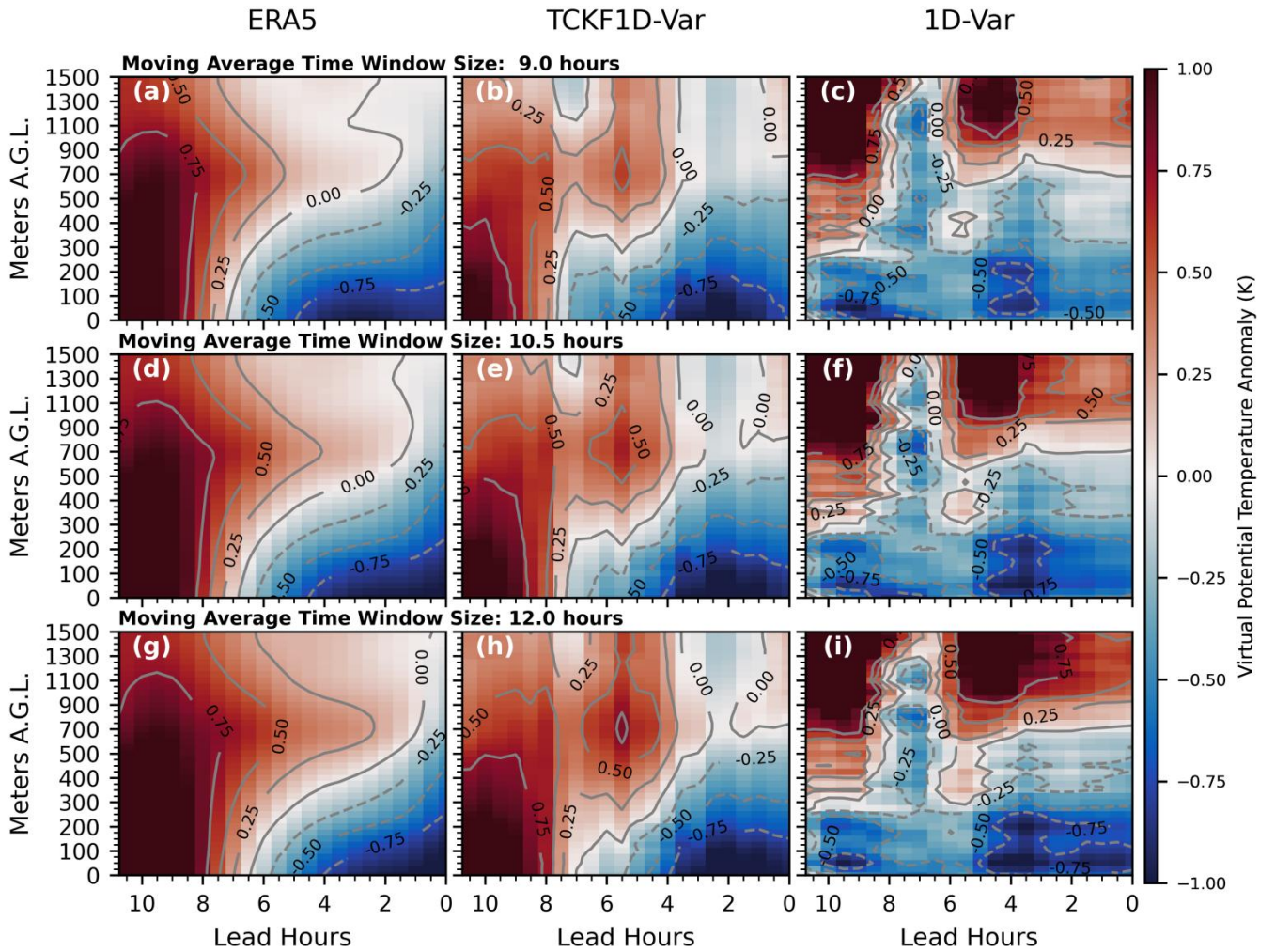
Figure 11. Case-averaged time–height evolution of virtual potential temperature anomalies derived from ERA5 (a, d, g), TCKF1D-Var (b, e, h), and 1D-Var (c, f, i) under different temporal averaging windows of 9.0-hour (a–c), 10.5-hour (d–f), and 12.0-hour (g–i), spanning from 11 h before to the onset of precipitation. ERA5 and TCKF1D-Var reveal the positive-to-negative anomaly transition below 400 m and the warm anomaly tongue intrusion between 400–1100 m, serving as precursors of heavy rainfall. Compared to ERA5, TCKF1D-Var provides stronger signals and longer lead times (7.5–8.0 h), whereas 1D-Var fails to capture these features and exhibits spurious anomaly layers under the −0.75 K criterion.

5 Summary and Concluding Remarks

This study introduces and evaluates TCKF1D-Var, a thermodynamic-constrained Kalman-filter/1D-variational framework to retrieve temperature, water vapor, and hydrometeor profiles from ground-based microwave radiometers (GMWRs). Designed to overcome classical 1D-Var weaknesses in cloudy conditions, TCKF1D-Var enforces moist-thermodynamic consistency and closes the retrieval with a simple single-moment microphysics (WSM3), linking the state vector to cloud liquid/ice water. Its cost function is reformulated as a dimensionless ratio, removing explicit dependence on climatological
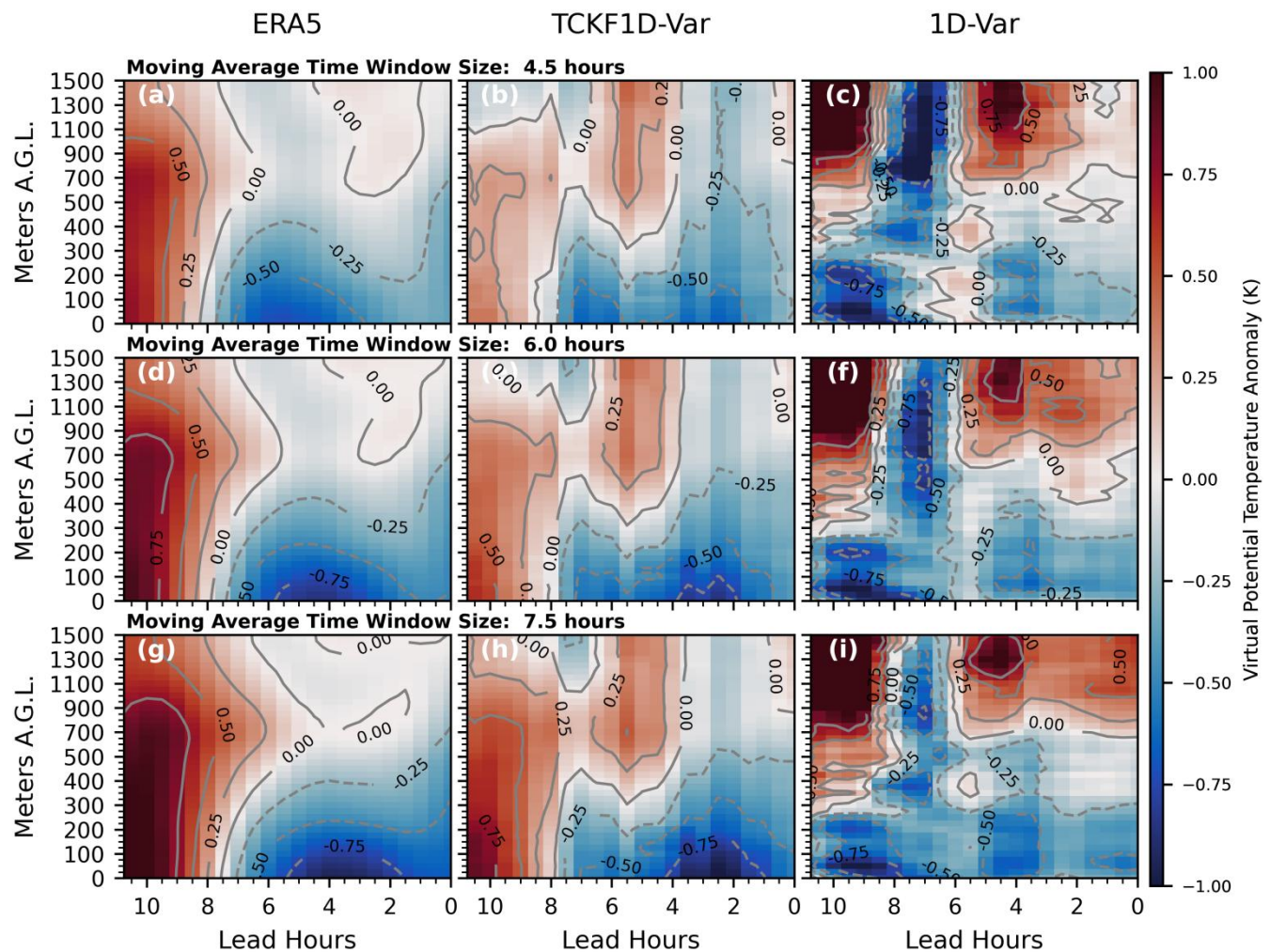
background and observation error covariances and preserving rapidly evolving signals. Key methodological innovations are:

410 (1) using virtual potential temperature (θ_v) as the control variable so temperature, humidity, pressure and hydrometeors adjust jointly under moist-adiabatic constraints; (2) adopting a ratio-based cost function to avoid suppressing transient features by mis-specified B/R matrices; and (3) adding a diagnostic microphysics closure to capture vertical hydrometeor structure when RTTOV-gb radiative transfer alone is insufficient.

415 A North China deployment of 44 GMWR sites (seven with collocated radiosondes) shows consistent gains. Relative to ERA5 and a classical 1D-Var, TCKF1D-Var substantially reduces systematic biases in temperature and humidity (largest temperature bias reductions above ~2 km; strongest humidity bias reductions from the surface to ~5.5 km). Temperature RMSE is comparable to ERA5 and lower than 1D-Var below ~8.5 km. Humidity RMSE is improved over 1D-Var in the near-surface layer (0–1.5 km) but is larger than ERA5 aloft—an issue diagnosed below. Hydrometeor validation against

420 collocated EarthCARE cloud liquid water content profiles (±15 min, 15 km; July 2025) finds TCKF1D-Var produces the smallest biases and lowest RMSE, and best reproduces EarthCARE distributions in the 36–136 mg·m^{-3} range. The collocation sample is modest and seasonally limited, so broader validation is needed. In application to eight short-duration extreme precipitation events (WMO ≥10 mm·h^{-1}), TCKF1D-Var strengthens precursory θ_v signals and lengthens first-alert lead time from ~6–7 h (ERA5) to ~7.5–8 h while retaining the ~4–4.5 h reconfirmation window; 1D-Var often fails to

425 capture robust precursors.

A focused "RMSE deficit" analysis attributes mid-tropospheric humidity degradation to vertical-resolution mismatch and cross-talk between oxygen (temperature-sensitive) and water-vapor channels: misaligned weighting-function peaks permit temperature uncertainty to leak into humidity retrievals, especially in the ~1.5–4.5 km layer. This highlights an intrinsic

430 limitation of passive microwave profiling and motivates explicit cross-covariance handling or multi-sensor synergy (e.g., lidar, cloud radar). We also acknowledge that the performance of the classical 1D-Var approach is inherently shaped by the prescribed background (B) and observation (R) error covariance matrices, and the differences highlighted in this study should not be interpreted as a universal limitation. Rather than positioning TCKF1D-Var as a replacement for 1D-Var, our intention is to provide a complementary retrieval framework that incorporates moist-thermodynamic constraints and a

435 microphysical closure, features that are not explicitly represented in the classical formulation. The evaluation sites in North China exhibit regional characteristics, and it is fully plausible that in regimes with weaker humidity gradients or reduced baroclinicity, 1D-Var may perform similarly or even more favourably. Radiosonde observations remain an essential benchmark for upper-air thermodynamic verification, and to address the limited availability of co-located soundings, additional comparisons with ERA5 were included. Overall, the combined evaluation suggests that TCKF1D-Var can extract

440 additional thermodynamic information from GMWR measurements and thus serves as a useful complement to existing 1D-

Var techniques under the conditions examined. These considerations have been incorporated to ensure that the inter-method comparison is presented within a balanced and context-appropriate framework.

Nevertheless, This study demonstrates that the TCKF1D-Var framework efficiently integrates thermodynamic constraints and microphysical closure into a unified variational retrieval system, substantially reducing biases, improving hydrometeor profile realism, and enhancing heavy-rain precursor detection. These results highlight its potential for continuous GMWR profiling and short-range nowcasting applications. However, current validation relies on about 60 collocated EarthCARE profiles from July 2025, which limits the statistical robustness of hydrometeor evaluation and the representativeness of seasonal variability. July was selected as the initial test period because the prevailing synoptic conditions over North China frequently give rise to a wide range of convective systems, providing a favorable environment for evaluation; nevertheless, extending the experimental period remains necessary to ensure more robust and statistically representative results. Future work will extend evaluations across seasons and regions, employ more advanced microphysics and Bayesian uncertainty quantification, and incorporate multi-sensor fusion and scattering-aware radiative operators to further improve retrieval robustness and operational applicability.

Appendix A: Sensitivity of Virtual Potential Temperature Anomaly to Temporal Averaging Window

Figuure A1. Case-averaged time–height evolution of virtual potential temperature anomalies derived from ERA5 (a, d, g), TCKF1D-Var (b, e, h), and 1D-Var (c, f, i) under reduced temporal averaging windows of 4.5-hour (a–c), 6.0-hour (d–f), and 7.5-hour (g–i). Compared to Fig. 10, anomaly gradients weaken with shorter windows; however, ERA5 and TCKF1D-Var still capture the positive-to-negative transition ~7–8 hours before rainfall onset and the warm anomaly tongue intrusion, albeit with reduced intensity. The −0.75 K early-warning signal is indistinct for the 4.5-hour window but becomes clearer and more temporally stable (~2 hours offset) for the 6.0 h and 7.5 h windows, while 1D-Var fails to provide effective precursors.

Code availability

Data availability

The input data required by the TCKF1D-Var framework are available on Zenodo (Zhang, 2025a; https://doi.org/10.5281/zenodo.17296305). The TCKF1D-Var thermodynamic and hydrometeor profile dataset generated in this study is also archived on Zenodo (Zhang, 2025b; https://doi.org/10.5281/zenodo.17083973). All datasets are publicly available under the Creative Commons Attribution 4.0 International (CC BY 4.0) license.

Author contribution

J.P.G. and T.M.C. planned the measurement campaign. T.M.C., Y.W., Y.W., J.J.Y. and B.D. conducted the ground-based observations. Q.Z. developed the TCKF1D-Var framework, performed the coding and data analysis, and prepared the manuscript. T.M.C. revised the manuscript. J.P.G., Q.Z., and T.M.C. provided funding.

Competing interests

The authors declare no conflicts of interests.

Acknowledgements

Financial support

References

Adler, B., J. M. Wilczak, L. Bianco, I. Djalalova, J. B. Duncan Jr., and D. D. Turner: Observational case study of a persistent cold air pool and gap flow in the Columbia River Basin. Journal of Applied Meteorology and Climatology, 60, 1071–1090, https://doi.org/10.1175/JAMC-D-21-0013.1, 2021.

Barrera-Verdejo, M., S. Crewell, U. Löhnert, E. Orlandi, and P. Di Girolamo: Ground-based lidar and microwave radiometry synergy for high vertical resolution absolute humidity profiling. Atmospheric Measurement Techniques, 9, 4013–4028, https://doi.org/10.5194/amt-9-4013-2016, 2016.

495 Bell, A., Martinet, P., Caumont, O., Vié, B., Delanoë, J., Dupont, J.-C., and Borderies, M.: W-band radar observations for fog forecast improvement: an analysis of model and forward operator errors, Atmos. Meas. Tech., 14, 4929–4946, https://doi.org/10.5194/amt-14-4929-2021, 2021.

Bell, B., Hersbach, H., Simmons, A., Berrisford, P., Dahlgren, P., Horányi, A., Muñoz-Sabater, J., Nicolas, J., Radu, R., Schepers, D., and Soci, C.: The ERA5 global reanalysis: Preliminary extension to 1950, Q. J. Roy. Meteor. Soc., 147, 4186–4227, https://doi.org/10.1002/qj.4174, 2021.

500 Benjamin, S. G., James, E. P., Hu, M., Alexander, C. R., Ladwig, T. T., Brown, J. M., Weygandt, S. S., Turner, D. D., Minnis, P., and Smith, W. L. Jr.: Stratiform cloud-hydrometeor assimilation for HRRR and RAP model short-range weather prediction, Monthly Weather Review, 149, 2673–2694, https://doi.org/10.1175/MWR-D-20-0385.1, 2021.

Byrd, R. H., Lu, P., Nocedal, J.; A Limited Memory Algorithm for Bound-Constrained Optimization. SIAM J. Sci. Stat. Comput., 16, 1190–1208, 1995.

505 Carminati, F.: A channel selection for the assimilation of CrIS and HIRAS instruments at full spectral resolution, Quarterly Journal of the Royal Meteorological Society, 148, 1092–1112, https://doi.org/10.1002/qj.4248, 2022.

Christofilakis, V., G. Tatsis, S. K. Chronopoulos, A. Sakkas, A. G. Skrivanos, K. P. Peppas, H. E. Nistazakis, G. Baldoumas, and P. Kostarakis: Earth-to-earth microwave rain attenuation measurements: A survey on the recent literature. Symmetry, 12, 1440, https://doi.org/10.3390/sym12091440, 2020.

510 Cimini, D., Hocking, J., De Angelis, F., Cersosimo, A., Di Paola, F., Gallucci, D., Gentile, S., Geraldi, E., Larosa, S., Nilo, S., Romano, F., Ricciardelli, E., Ripepi, E., Viggiano, M., Luini, L., Riva, C., Marzano, F. S., Martinet, P., Song, Y. Y., Ahn, M. H., and Rosenkranz, P. W.: RTTOV-gb v1.0 – updates on sensors, absorption models, uncertainty, and availability, Geosci. Model Dev., 12, 1833–1845, https://doi.org/10.5194/gmd-12-1833-2019, 2019.

De Angelis, F., Cimini, D., Hocking, J., Martinet, P., and Kneifel, S.: RTTOV-gb – adapting the fast radiative transfer model

515 RTTOV for the assimilation of ground-based microwave radiometer observations, Geosci. Model Dev., 9, 2721–2739, https://doi.org/10.5194/gmd-9-2721-2016, 2016.

de Haan, S. and van der Veen, S. H.: Cloud initialization in the Rapid Update Cycle of HIRLAM, Weather and Forecasting, 29, 1120–1133, https://doi.org/10.1175/WAF-D-13-00071.1, 2014.

Donovan, D. P., Barker, H. W., Hogan, R. J., Wehr, T., Eisinger, M., Lajas, D., Lefebvre, A., and EarthCARE Phase-B

520 ESA/JAXA Mission Advisory Group: Scientific aspects of the Earth Clouds, Aerosols, and Radiation Explorer (EarthCARE) mission, AIP Conf. Proc., 1531, 444–447, https://doi.org/10.1063/1.4804793, 2013.

Ebell, K., U. Löhnert, E. Päschke, E. Orlandi, J. H. Schween, and S. Crewell: A 1-D variational retrieval of temperature, humidity, and liquid cloud properties: performance under idealized and real conditions. Journal of Geophysical Research: Atmospheres, 122, 1746–1766, https://doi.org/10.1002/2016JD025945, 2017.

525   Esri, DeLorme, HERE, TomTom, Intermap, increment P Corp., GEBCO, USGS, FAO, NPS, NRCAN, GeoBase, IGN, Kadaster NL, Ordnance Survey, Esri Japan, METI, Esri China (Hong Kong), swisstopo, MapmyIndia, the GIS User Community: World Imagery, https://www.arcgis.com/home/item.html?id=10df2279f9684e4a9f6a7f08febac2a9, 2025.

European Space Agency: EarthCARE CPR CLD Level 2A (version AB) Dataset, https://doi.org/10.57780/eca-e6471c5, 2025.

530   Foth, A. and Pospichal, B.: Optimal estimation of water vapour profiles using a combination of Raman lidar and microwave radiometer, Atmospheric Measurement Techniques, 10, 3325–3344, https://doi.org/10.5194/amt-10-3325-2017, 2017.

Gamage, S. M., Sica, R. J., Martucci, G., and Haefele, A.: A 1D-Var retrieval of relative humidity using the ERA5 dataset for the assimilation of Raman lidar measurements, Journal of Atmospheric and Oceanic Technology, 37, 2051–2064, https://doi.org/10.1175/JTECH-D-19-0170.1, 2020.

535   Garcia-Carreras, L., Parker, D. J., Taylor, C. M., Reeves, C. E., and Murphy, J. G.: Impact of mesoscale vegetation heterogeneities on the dynamical and thermodynamic properties of the planetary boundary layer, J. Geophys. Res., 115, D03102, https://doi.org/10.1029/2009JD012811, 2010.

Geerts, B., D. Parsons, C. Ziegler, T. Weckwerth, M. Biggerstaff, R. Clark, M. Coniglio, B. Demoz, R. Ferrare, W. Gallus Jr., et al.: The 2015 Plains Elevated Convection At Night field project. Bulletin of the American Meteorological Society, 98, 540   767–786, https://doi.org/10.1175/BAMS-D-15-00257.1, 2017.

Hersbach, H., Bell, B., Berrisford, P., et al.: The ERA5 global reanalysis, Q. J. Roy. Meteor. Soc., 146, 1999–2049, https://doi.org/10.1002/qj.3803, 2020.

Hewison, T. J. and Gaffard, C.: 1D-Var retrieval of temperature and humidity profiles from ground-based microwave radiometers, 2006 IEEE MicroRad, San Juan, Puerto Rico, USA, 28 February–3 March 2006, 235–240, 545   https://doi.org/10.1109/MICRAD.2006.1677095, 2006.

Hewison, T. J.: 1D-VAR retrieval of temperature and humidity profiles from a ground-based microwave radiometer, IEEE Trans. Geosci. Remote Sens., 45, 2163–2168, https://doi.org/10.1109/TGRS.2007.898091, 2007.

Hoffmann, L., Günther, G., Li, D., Stein, O., Wu, X., Griessbach, S., Heng, Y., Konopka, P., Müller, R., Vogel, B., and Wright, J. S.: From ERA-Interim to ERA5: The considerable impact of ECMWF's next-generation reanalysis on Lagrangian 550   transport simulations, Atmos. Chem. Phys., 19, 3097–3124, https://doi.org/10.5194/acp-19-3097-2019, 2019.

Hong, S.-Y., Dudhia, J., and Chen, S.-H.: A revised approach to ice microphysical processes for the bulk parameterization of clouds and precipitation, Mon. Weather Rev., 132, 103–120, https://doi.org/10.1175/1520-0493(2004)132<0103:ARATIM>2.0.CO;2, 2004.

Hu, J., N. Yussouf, D. D. Turner, T. A. Jones, and X. Wang: Impact of ground-based remote sensing boundary layer 555   observations on short-term probabilistic forecasts of a tornadic supercell event. Weather and Forecasting, 34, 1453–1476, https://doi.org/10.1175/WAF-D-18-0200.1, 2019.

Hélière, A., Wallace, K., Pereira Do Carmo, J., and Lefebvre, A.: Earth cloud, aerosol, and radiation explorer optical payload development status, Proc. SPIE, Sensors, Systems, and Next-Generation Satellites XXI, 10423, 8–25, https://doi.org/10.1117/12.2274704, 2017.

560 Imura, Y., Tomita, E., Nio, T., Okada, K., Maruyama, K., Nakatsuka, H., Tomiyama, N., Aida, Y., Haze, K., Ochiai, S., Konoue, K., Kubota, T., Tanaka, T., Muto, M., Aoki, S., Horie, H., Ohno, Y., and Sato, K.: EarthCARE/CPR current conditions and preliminary results from scientific views, Proc. SPIE, Remote Sensing of the Atmosphere, Clouds, and Precipitation VIII, 13262, 1326202, https://doi.org/10.1117/12.3045833, 2025.

Kimura, T., Kondo, K., Kumagai, H., Kuroiwa, H., Ishida, C., Oki, R., and Nakajima, T.: EarthCARE – Earth Clouds,
565 Aerosol, and Radiation Explorer: its objectives and Japanese sensor designs, Proc. SPIE, Remote Sensing of Clouds and the Atmosphere VII, 4882, 510–519, https://doi.org/10.1117/12.469725, 2003.

Kummerow, C., Olson, W. S., and Giglio, L.: A simplified scheme for obtaining precipitation and vertical hydrometeor profiles from passive microwave sensors, IEEE Trans. Geosci. Remote Sens., 34, 1213–1232, https://doi.org/10.1109/36.536538 , 2022.

570 Larosa, S., Cimini, D., Gallucci, D., Nilo, S. T., and Romano, F.: PyRTlib: an educational Python-based library for non-scattering atmospheric microwave radiative transfer computations, Geosci. Model Dev., 17, 2053–2076, https://doi.org/10.5194/gmd-17-2053-2024, 2024.

Li, Q., M. Wei, Z. Wang, and Y. Chu: Evaluation and improvement of the quality of ground-based microwave radiometer clear-sky data. Atmosphere, 12, 435, https://doi.org/10.3390/atmos12040435, 2021.

575 Liu, D. and C. Nocedal, J.: On the Limited Memory Method for Large Scale Optimization. Math. Program., 45B, 503–528, 1989.

Löhnert, U. and Maier, O.: Operational profiling of temperature using ground-based microwave radiometry at Payerne: prospects and challenges, Atmos. Meas. Tech., 5, 1121–1134, https://doi.org/10.5194/amt-5-1121-2012, 2012.

Löhnert, U., and O. Maier: Operational profiling of temperature using ground-based microwave radiometry at Payerne:
580 prospects and challenges. Atmospheric Measurement Techniques, 5, 1121–1134, https://doi.org/10.5194/amt-5-1121-2012, 2012.

Martinet, P., Cimini, D., De Angelis, F., Canut, G., Unger, V., Guillot, R., Tzanos, D., and Paci, A.: Combining ground-based microwave radiometer and the AROME convective scale model through 1DVAR retrievals in complex terrain: an Alpine valley case study, Atmos. Meas. Tech., 10, 3385–3402, https://doi.org/10.5194/amt-10-3385-2017, 2017.

585 Mason, S. L., Barker, H. W., Cole, J. N. S., Docter, N., Donovan, D. P., Hogan, R. J., Hünerbein, A., Kollias, P., Puigdomènech Treserras, B., Qu, Z., Wandinger, U., and van Zadelhoff, G.-J.: An intercomparison of EarthCARE cloud, aerosol, and precipitation retrieval products, Atmos. Meas. Tech., 17, 875–898, https://doi.org/10.5194/amt-17-875-2024, 2024.

Mroz, K., Treserras, B. P., Battaglia, A., Kollias, P., Tatarevic, A., and Tridon, F.: Cloud and precipitation microphysical retrievals from the EarthCARE Cloud Profiling Radar: the C-CLD product, Atmos. Meas. Tech., 16, 2865–2888, https://doi.org/10.5194/amt-16-2865-2023, 2023.

NOAA: U.S. Standard Atmosphere, National Oceanic and Atmospheric Administration, Washington, D.C., USA, 1976.

Noh, Y., Huang, H., and Goldberg, M. D.: Refinement of CrIS channel selection for global data assimilation and its impact on the global weather forecast, Weather and Forecasting, 36, 1405–1429, https://doi.org/10.1175/WAF-D-21-0002.1, 2021.

Que, L. J., Que, W. L., and Feng, J. M.: Intercomparison of different physics schemes in the WRF model over the Asian summer monsoon region, Atmos. Oceanic Sci. Lett., 9, 169–177, https://doi.org/10.1080/16742834.2016.1158618, 2016.

Rodgers, C. D.: Inverse methods for atmospheric sounding: Theory and practice. Vol. 2. World Scientific, ISBN 981022740X, 2000.

Taylor, C. M., Parker, D. J., and Harris, P. P.: An observational case study of mesoscale atmospheric circulations induced by soil moisture, Geophys. Res. Lett., 34, L15801, https://doi.org/10.1029/2007GL030572, 2007.

Teixeira, J., J. R. Piepmeier, A. R. Nehrir, C. O. Ao, S. S. Chen, C. A. Clayson, A. M. Fridlind, M. Lebsock, W. McCarty, H. Salmun, et al.: Toward a global planetary boundary layer observing system: A summary. Bulletin of the American Meteorological Society, https://doi.org/10.1175/BAMS-D-23-0228.1, 2025.

Thelen, J.-C., Havemann, S., Newman, S.M. and Taylor, J.P.: Hyperspectral retrieval of land surface emissivities using ARIES. Q.J.R. Meteorol. Soc., 135: 2110-2124. https://doi.org/10.1002/qj.520, 2009.

Turner, D. D., and U. Löhnert: Ground-based temperature and humidity profiling: combining active and passive remote sensors. Atmospheric Measurement Techniques, 14, 3033–3048, https://doi.org/10.5194/amt-14-3033-2021, 2021.

Viggiano, M., Cimini, D., De Natale, M. P., Di Paola, F., Gallucci, D., Larosa, S., and Romano, F.: Combining passive infrared and microwave satellite observations to investigate cloud microphysical properties: A review. Remote Sens., 17, 337, https://doi.org/10.3390/rs17020337, 2025.

Wagner, T. J., P. M. Klein, and D. D. Turner: A new generation of ground-based mobile platforms for active and passive profiling of the boundary layer. Bulletin of the American Meteorological Society, 100, 137–153, https://doi.org/10.1175/BAMS-D-17-0165.1, 2019.

Wang, K.-N., Ao, C. O., Morris, M. G., Hajj, G. A., Kurowski, M. J., Turk, F. J., and Moore, A. W.: Joint 1DVar retrievals of tropospheric temperature and water vapor from Global Navigation Satellite System radio occultation (GNSS-RO) and microwave radiometer observations, Atmos. Meas. Tech., 17, 583–599, https://doi.org/10.5194/amt-17-583-2024, 2024.

Weisz, E., W. L. Smith Sr., and N. Smith: Advances in simultaneous atmospheric profile and cloud parameter regression-based retrieval from high-spectral resolution radiance measurements. Journal of Geophysical Research: Atmospheres, 118, 6433–6443, https://doi.org/10.1002/jgrd.50521, 2013.

Welch, G. and Bishop, G.: An introduction to the Kalman filter, University of North Carolina at Chapel Hill, Department of Computer Science, Technical Report TR 95-041, 16 pp, 1995.

World Meteorological Organization (WMO): WMO Technical Document No. 1390, https://library.wmo.int/viewer/40422/?offset=#page=1&viewer=picture&o=bookmark&n=0&q=, 2007.

Wulfmeyer, V., R. M. Hardesty, D. D. Turner, A. Behrendt, M. Cadeddu, P. Di Girolamo, P. Schluessel, J. van Baelen, and F. Zus: A review of the remote sensing of lower-tropospheric thermodynamic profiles and its indispensable role for the understanding and simulation of water and energy cycles. Reviews of Geophysics, 53, 819–895, https://doi.org/10.1002/2014RG000476 ,2015.

Xu, G.: A review of remote sensing of atmospheric profiles and cloud properties by ground-based microwave radiometers in central China. Remote Sensing, 16, 966, https://doi.org/10.3390/rs16060966, 2024.

Yao, L., Shen, D., Sun, X., Wang, D., Cao, X., Wang, J., Wang, D., Zhang, C., and Guo, Q.: The Beidou Navigation Radiosonde Observation Experiment and Data Evaluation, SSRN [preprint], https://doi.org/10.2139/ssrn.5085235, 2025.

Zhang, L., Ma, Y., Lei, L., Wang, Y., Jin, S., and Gong, W.: Improving atmospheric temperature and relative humidity profiles retrieval based on ground-based multichannel microwave radiometer and millimeter-wave cloud radar. Atmosphere, 15, 1064, https://doi.org/10.3390/atmos15091064, 2024.

Zhang, Q., Smith, W. Sr., and Shao, M.: The potential of monitoring carbon dioxide emission in a geostationary view with the GIIRS meteorological hyperspectral infrared sounder, Remote Sensing, 15, 886, https://doi.org/10.3390/rs15040886, 2023.

Zhang, Q.: Input Data for TCKF1D-Var framework, Zenodo, https://doi.org/10.5281/zenodo.17296305, 2025.

Zhang, Q.: TCKF1D-Var framework, Zenodo, https://doi.org/10.5281/zenodo.17293102, 2025.

Zhang, Q.: TCKF1D-Var thermodynamic and hydrometeor profile dataset, Zenodo, https://doi.org/10.5281/zenodo.17083973, 2025.

Zhang, Y., Chen, S., Tan, W., Chen, S., Chen, H., Guo, P., Sun, Z., Hu, R., Xu, Q., Zhang, M., Hao, W., and Bu, Z.: Retrieval of Water Cloud Optical and Microphysical Properties from Combined Multiwavelength Lidar and Radar Data, Remote Sens., 13(21), 4396. https://doi.org/10.3390/rs13214396, 2021.